Received: 30 November 2022 | Revised: 4 April 2023 | Accepted: 5 April 2023

IET Microwaves, Antennas & Propagation

DOI: 10.1049/mia2.12365

ORIGINAL RESEARCH

Three-dimensional single-shell dielectric lens design using complex coordinates and local axis-displaced confocal quadrics

Aline Rocha de Assis[1] | **José Ricardo Bergmann**[2] | **Fernando José da Silva Moreira**[3]

[1]Departamento de Engenharia Elétrica, Universidade Federal de Ouro Preto (UFOP), João Monlevade, Minas Gerais, Brazil

[2]CETUC, Pontifícia Universidade Católica do Rio de Janeiro (PUC-Rio), Rio de Janeiro, Brazil

[3]Departamento de Engenharia Elétrica, Universidade Federal de Minas Gerias (UFMG), Belo Horizonte, Minas Gerais, Brazil

Correspondence

José Ricardo Bergmann.
Email: bergmann@puc-rio.br

Funding information

Coordenação de Aperfeiçoamento de Pessoal de Nível Superior, Grant/Award Number: 068419/2014-01; Conselho Nacional de Desenvolvimento Científico e Tecnológico, Grant/Award Numbers: 311249/2021-3, 303257/2022-9

Abstract

This study proposes an analytical formulation in complex coordinates to synthesise three-dimensional single-shell dielectric lens surfaces. An exact formulation based on geometrical optics is developed, and the synthesis problem is modelled as a non-linear second-order partial differential equation of the Monge–Ampère (MA) type. An alternative numerical scheme based on axis-displaced confocal quadrics is used to locally represent the surface of dielectric lens. The advantage of this approach is to analytically obtain the partial derivatives present in the MA equation. To validate the proposed methodology, numerical results are obtained by an iterative algorithm that allows the simultaneous control of the transmitted beam width and the power density amplitude in the far-field region. To illustrate the synthesis effectiveness, two examples of lens antennas are simulated and analysed.

KEYWORDS

lenses, optical design techniques, shaped beam antennas

1 | INTRODUCTION

In recent years, several works have proposed the use of dielectric lenses to design antennas for microwave and millimetre wave applications [1–4]. In these frequency ranges, conventional dielectric lenses can be designed to be small and low-weighted, increasing the set of lenses' advantages. These antennas are quite inexpensive, have good fabrication tolerances, wide-band capabilities, as well as very low dissipative losses. In this scenario, it is expected that proper modelling of dielectric lenses' surfaces may yield designs capable of assisting telecommunication services demanding higher data rates at increasingly higher frequencies.

In order to improve the performance of dielectric lenses in attaining desired radiation patterns, many aspects have been investigated as primary-feed reconfigurability, new dielectric materials (homogeneous dielectrics and metamaterials), and modelling of lenses' surfaces [4, 5].

By using geometrical optics (GO) principles, the problem of modelling reflectors' surfaces to obtain contoured beams in the antenna far-field region was successfully formulated for single and dual reflector antennas [6–8], leading to a non-linear partial differential equation of the Monge–Ampère (MA) type. To control the power and phase aperture distributions, the synthesis of double surface lenses was formulated by employing a similar approach [9]. A relevant work was conducted in Ref. [5], where a non-linear partial differential equation of the MA type was derived in spherical coordinates to design homogeneous dielectric lenses of arbitrary shapes. In Ref. [5], a scheme based on finite differences was employed to numerically solve the MA equation. Three-dimensional dielectric lenses were successfully designed after fine refinements attained by a physical optics (PO) optimisation algorithm. However, in Ref. [5] its formulation does not take advantage of the simplifications allowed by the elegant ray-direction representation in terms of stereographic projections [6–9].

To simplify the mathematics involved in the MA equation for lenses' design, this work follows the steps presented in Ref. [9] and derives it compactly and elegantly by using complex coordinates. The formalism employs stereographic projections to represent the directions of incident and refracted rays through a dielectric interface, and no geometric symmetries are assumed. Differently from Ref. [9], an alternative methodology is applied to the numerical solution of the MA equation: Axis displaced confocal quadrics locally represent the dielectric surfaces [10, 11]. This approach allows the MA equation derivatives to be analytically represented, avoiding the use of finite differences or similar methodologies. To illustrate the effectiveness of the synthesis procedure, this study is organised as follows. Initially, it presents a summary of the complex coordinates' notation employed in the synthesis formulation and the derivation of the corresponding MA equation. For the numerical solution, a boundary condition is specified at the rims of the incident and refracted GO beams. A strategy to deal with reflection losses at the dielectric surface is discussed. To validate the algorithm, two examples of GO modelled dielectric lenses are synthesised and analysed by a GO-PO scheme.

2 | COMPLEX COORDINATES AND GEOMETRY OF THE SYNTHESIS PROBLEM

In this section, we follow the method presented in Ref. [9], and we highlight the main expressions necessary to describe the synthesis problem. Let P(x, y, z) denote a general point over a unit sphere of centre O, the origin of the coordinate system (see Figure 1). Consider P′(u, v, 0) the stereographic projection of P from Q(0, 0, 1) at plane $z = 0$. The complex coordinate η associated with the usual spherical coordinates θ and ϕ of P is defined as

$$\eta = u + jv = \cot\left(\frac{\theta}{2}\right)\exp(j\phi) \tag{1}$$

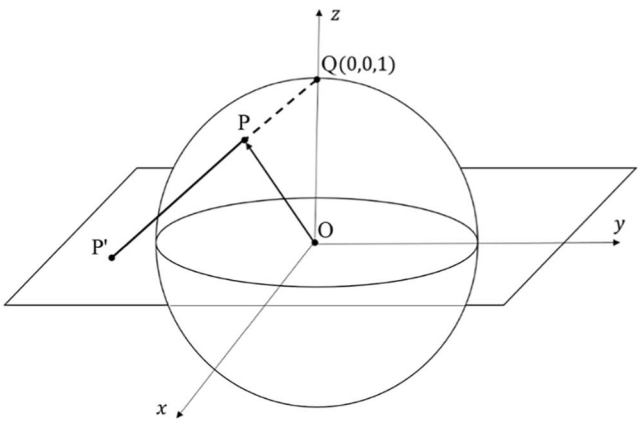

FIGURE 1 Stereographic projection of a point P on the plane xy.

Furthermore, an arbitrary vector $\vec{a}$ with rectangular components (a_x, a_y, a_z) is represented as ($a_x + ja_y$, a_z) [6–9]. Using this shorten notation, a unit vector $\hat{p} = \overrightarrow{OP}/\left|\overrightarrow{OP}\right|$ pointing in the direction (θ, ϕ) can be written using the complex coordinate η and its modulus $|\eta|$ as

$$\hat{p}(\eta) = \left(\frac{2\eta}{|\eta|^2+1}, \frac{|\eta|^2-1}{|\eta|^2+1}\right) \tag{2}$$

Figure 2 illustrates an incident ray from a source point O (origin of the coordinate system) that is refracted at a point R over a dielectric interface. The directions of the incident and refracted rays are represented by the complex coordinates η and ζ, respectively. The corresponding unit vectors in the incident and refracted directions are $\hat{p}(\eta)$ and $\hat{t}(\zeta)$, respectively. Both mediums are homogeneous, and their refraction indices are $N > 1$ (for the incidence region) and one (refraction region) in which case one should care for critical angles (i.e. total reflection).

To apply GO principles for the synthesis of the lens surface, a real function

$$L(\eta) = \ln\left(\frac{r(\eta)}{1+|\eta|^2}\right) \tag{3}$$

is conveniently defined to represent the dielectric surface $r(\eta)$ [9]. Afterwards, the application of Snell's Law of refraction yields the derivative of $L(\eta)$ with respect to η as [9]:

$$L_\eta = \frac{2\left(\overline{\zeta}-\overline{\eta}\right) + \overline{\eta}(1-N)\left(1+|\zeta|^2\right)}{2|\zeta-\eta|^2 + (1-N)\left(1+|\eta|^2\right)\left(1+|\zeta|^2\right)} \tag{4}$$

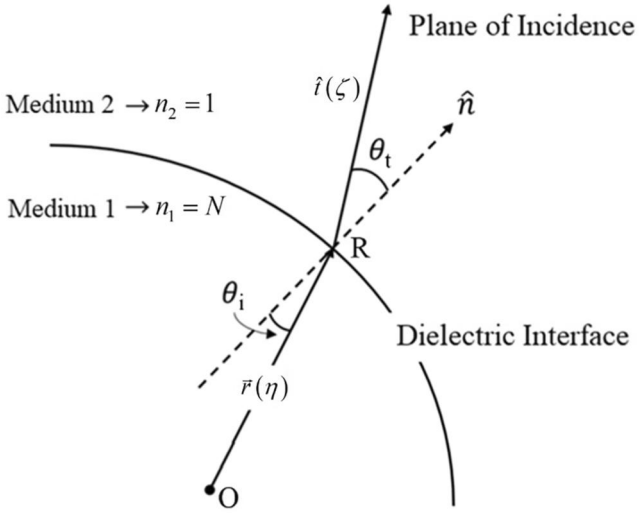

FIGURE 2 Geometry of the synthesis problem.

where $\overline{\eta}$ and $\overline{\zeta}$ represent the complex conjugates of η and ζ, respectively. Consequently, $|\eta|^2 = \eta\overline{\eta}$ and $|\zeta|^2 = \zeta\overline{\zeta}$. Equation (4) also provides the relation between the incident and the refracted ray directions from which one can derive a mapping function between η and ζ, [9]:

$$\zeta = \frac{(1+N)\eta L_\eta + (1-N)\overline{\eta}L_{\overline{\eta}} + 1 - \sqrt{1+\left(1-N^2\right)\left|\overline{\eta} + \left(1+|\eta|^2\right)L_\eta\right|^2}}{(1+N)L_\eta - (1-N)\overline{\eta}\left(1+\overline{\eta}L_{\overline{\eta}}\right)} \tag{5}$$

The mapping is not arbitrary and must satisfy an integrability condition [6–9], which demands the second derivative $L_{\eta\overline{\eta}}$ to be real and will be explicitly derived as follows. Equation (5) can be rewritten as

$$L_\eta = \partial S/\partial\eta = S_\eta(\eta,\zeta) \tag{6}$$

where

$$S(\eta,\zeta) = -\ln[E(\eta,\zeta)] \tag{7}$$

is a real valued function with

$$E(\eta,\zeta) = (N-1)\left(1+|\eta|^2\right)\left(1+|\zeta|^2\right) + 2|\zeta-\eta|^2 \tag{8}$$

In Equation (7), $E > 0$ because $N > 1$. One can then obtain the second-order derivatives of S as:

$$S_{\eta\zeta} = -2(1+N)\left(\overline{\zeta}-\overline{\eta}\right)^2/E^2, \tag{9a}$$

$$S_{\eta\overline{\zeta}} = -2(1-N)(1+\zeta\overline{\eta})^2/E^2 \tag{9b}$$

$$S_{\eta\eta} = S_\eta^2 = L_\eta^2, \tag{9c}$$

$$S_{\eta\overline{\eta}} = \left(1-N^2\right)\left(1+|\zeta|^2\right)^2/E^2. \tag{9d}$$

Applying the chain rule to Equation (6), one can show that

$$L_{\eta\overline{\eta}} - S_{\eta\overline{\eta}} = S_{\eta\zeta}\,\zeta_{\overline{\eta}} + S_{\eta\overline{\zeta}}\,\overline{\zeta}_{\overline{\eta}}. \tag{10}$$

Finally, the integrability condition is imposed by forcing

$$S_{\eta\zeta}\,\zeta_{\overline{\eta}} + S_{\eta\overline{\zeta}}\,\overline{\zeta}_{\overline{\eta}} = (1+N)\left(\overline{\zeta}-\overline{\eta}\right)^2\zeta_{\overline{\eta}} + (1-N)(1+\zeta\overline{\eta})^2\overline{\zeta}_{\overline{\eta}} \tag{11}$$

to be real valued function, since the left hand side of Equation (11) is real by definition.

3 | ENERGY CONSERVATION: MONGE-AMPÈRE EQUATION

Let $I(\eta)$ and $G(\zeta)$ represent the power densities per solid angle emanating from the source point O and at the lens far-field region, respectively. Comparing the elementary areas subtended for cone rays over a unity sphere with centre O and assuming that all incident power is transmitted through the dielectric interface, it can be shown that [6–9].

$$\frac{I(\eta)}{G(\zeta)} = \left(\frac{1+|\eta|^2}{1+|\zeta|^2}\right)^2\left||\zeta_\eta|^2 - |\zeta_{\overline{\eta}}|^2\right| \tag{12}$$

where $|\zeta_\eta|^2 - |\zeta_{\overline{\eta}}|^2$ is the Jacobian of the mapping function Equation (5). The partial derivatives ζ_η and $\zeta_{\overline{\eta}}$ are attained by manipulating Equations (7)–(12) to obtain the following system of equations:

$$\begin{bmatrix} L_{\eta\eta} - S_{\eta\eta} & L_{\eta\overline{\eta}} - S_{\eta\overline{\eta}} \\ L_{\eta\overline{\eta}} - S_{\eta\overline{\eta}} & L_{\overline{\eta}\overline{\eta}} - S_{\overline{\eta}\overline{\eta}} \end{bmatrix} = \begin{bmatrix} p & q \\ \overline{q} & \overline{p} \end{bmatrix}\begin{bmatrix} \zeta_\eta & \zeta_{\overline{\eta}} \\ \overline{\zeta}_\eta & \overline{\zeta}_{\overline{\eta}} \end{bmatrix} \tag{13}$$

where $p = S_{\eta\zeta}$ and $q = S_{\eta\overline{\zeta}}$. From the determinants of both sides of Equation (13) one has

$$\left|L_{\eta\eta} - S_{\eta\eta}\right|^2 - \left(L_{\eta\overline{\eta}} - S_{\eta\overline{\eta}}\right)^2 = \left(|p|^2 - |q|^2\right)\left(|\zeta_\eta|^2 - |\zeta_{\overline{\eta}}|^2\right). \tag{14}$$

The substitution of the energy conservation Equations (12) into (14) leads to the desired MA differential equation:

$$\left|L_{\eta\eta} - L_\eta^2\right|^2 - \left(L_{\eta\overline{\eta}} - B(\eta,\zeta)\right)^2 = \pm H(\eta,\zeta) \tag{15}$$

where

$$B(\eta,\zeta) = S_{\eta\overline{\eta}} = \frac{\left(1-N^2\right)\left(1+|\zeta|^2\right)^2}{\left[(N-1)\left(1+|\eta|^2\right)\left(1+|\zeta|^2\right) + 2|\zeta-\eta|^2\right]^2} \tag{16}$$

$$H(\eta,\zeta) = V(\eta,\zeta)\frac{I(\eta)}{G(\zeta)}\left(\frac{1+|\zeta|^2}{1+|\eta|^2}\right)^2 \tag{17}$$

$$V(\eta,\zeta) = |p|^2 - |q|^2 = \frac{4\left[(1+N)^2\left|\overline{\zeta}-\overline{\eta}\right|^4 - (1-N)^2\left|1+\eta\overline{\zeta}\right|^4\right]}{\left[(N-1)\left(1+|\eta|^2\right)\left(1+|\zeta|^2\right)+2|\zeta-\eta|^2\right]^4} \tag{18}$$

and $S_{\eta\eta} = (S_\eta)^2 = (L_\eta)^2$. One can show that $V < 0$ and, consequently, the MA equation is of the elliptic (hyperbolic) type for the + (−) sign in Equation (15). It is important to highlight that the surface represented by $L(\eta)$ describes a dielectric lens of arbitrary shapes, without any kind of symmetry. Moreover, Equation (15) does not consider reflection losses at the dielectric interface. Although some initial steps are similar to those of [9], the present MA equation is different from that of [9]. There, the authors shape a dual surface lens to control the power distribution in an aperture placed in front of the lens, while here a single surface (interface) is used to control the radiated power.

4 | BOUNDARY CONDITIONS

The MA Equation (15) is to be solved as a boundary value problem. For that, it is assumed that the source point O radiates a conical tube of rays with semi-angle θ_c with respect to the negative z-direction, as illustrated in Figure 3. The conical tube of rays and the far-field coverage area are placed in the z-negative semi space to avoid singularities of the complex coordinates at the positive z-axis. The boundary condition enforces the incident rays at the cone θ_c (i.e. cross section rim) to map, after refraction, into points at the given far-field contour Ω. In the present work, such contour is defined as a superellipse, described by Ref. [12]:

$$\rho(\zeta,\overline{\zeta}) = \left|\cot\left(\frac{\alpha_x}{2}\right)\left(\frac{\zeta+\overline{\zeta}}{2}\right)\right|^{2\sigma} + \left|\cot\left(\frac{\alpha_y}{2}\right)\left(\frac{\zeta-\overline{\zeta}}{2}\right)\right|^{2\sigma} \tag{19}$$

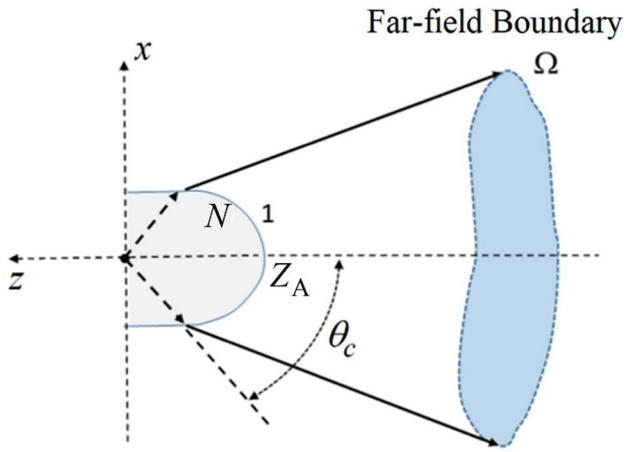

FIGURE 3 Geometry of the dielectric lens antenna as a boundary value problem.

where α_x and α_y are the far-field beamwidths in the xz- and yz-planes, respectively. For $\sigma = 1$, the contour Ω becomes an ellipse and for $\sigma \to \infty$, Ω tends to a rectangle.

5 | NUMERICAL SOLUTION

It is well established that MA equations can be numerically solved as boundary value problems by linearising these equations and stablishing an initial approximation (Newton's method). To apply this technique, Equation (15) is rewritten in the following operator form:

$$\Gamma(L) = \left|L_{\eta\eta} - L_\eta^2\right|^2 - \left(L_{\eta\overline{\eta}} - B(\eta,\zeta)\right)^2 \pm H(\eta,\zeta) = 0 \tag{20}$$

For its numerical solution, an alternative methodology is employed, which uses axis displaced confocal quadrics to locally represent the dielectric surface. Consequently, the derivatives of the MA equation can be analytically represented. Such approach was successfully used to synthesise single and offset reflectors [10, 11].

Once the displaced confocal quadrics are represented by closed analytical forms in complex coordinates, their derivatives are easily obtained [10]. Under this approach, L_η is known and substituting it into Equation (5), the mapping function $\eta \to \zeta$ can be obtained analytically. Furthermore, it is important to highlight that the term $\left|L_{\eta\eta} - L_\eta^2\right|$ in Equations (15) and (20) becomes zero for quadric surfaces [10], yielding an important simplification of the MA operator $\Gamma(L)$:

$$\Gamma(L) = \left(L_{\eta\overline{\eta}} - B(\eta,\zeta)\right)^2 \mp H(\eta,\zeta) = 0 \tag{21}$$

For domain discretisation, a polar grid with J rings and K radials was adopted. So, Equation (21) can be rewritten for discrete points (j,k) mapped inside the far-field cross section limited by Ω as

$$\Gamma(L_{j,k}) = \left[L_{\eta\overline{\eta}}\left(a_{j,k}, b_{j,k}, c_{j,k}, d_{j,k}, \eta_{j,k}\right) - B\left(\eta_{j,k}, \zeta_{j,k}\right)\right]^2 \mp H\left(\eta_{j,k}, \zeta_{j,k}\right) = 0 \tag{22}$$

where $a_{j,k}$, $b_{j,k}$, $c_{j,k}$, $d_{j,k}$ are the coefficients that define the confocal quadrics with a centre point indexed at (j,k) [10, 11]. For contour points $(j = J)$ at Ω, the operator is defined to satisfy the boundary condition Equation (20) as

$$\Gamma(L_{J,k}) = 1 - \left|\cot\left(\frac{\alpha_x}{2}\right)\left(\frac{\zeta_{J,k}+\overline{\zeta}_{J,k}}{2}\right)\right|^{2\sigma} - \left|\cot\left(\frac{\alpha_y}{2}\right)\left(\frac{\zeta_{J,k}-\overline{\zeta}_{J,k}}{2}\right)\right|^{2\sigma} \tag{23}$$

Then, using an iterative procedure, the initial solution converges to the desired surface that is now represented by a set of confocal quadrics locally describing the desired lens surface.

6 | REFLECTION LOSSES

The previous formulation does not consider reflection losses at the dielectric interface. By applying the GO-PO approximation described in Ref. [5] for the analysis of the synthesised surface, it is possible to evaluate the power density radiated by the lens considering reflections at the interface and leading to the following distribution:

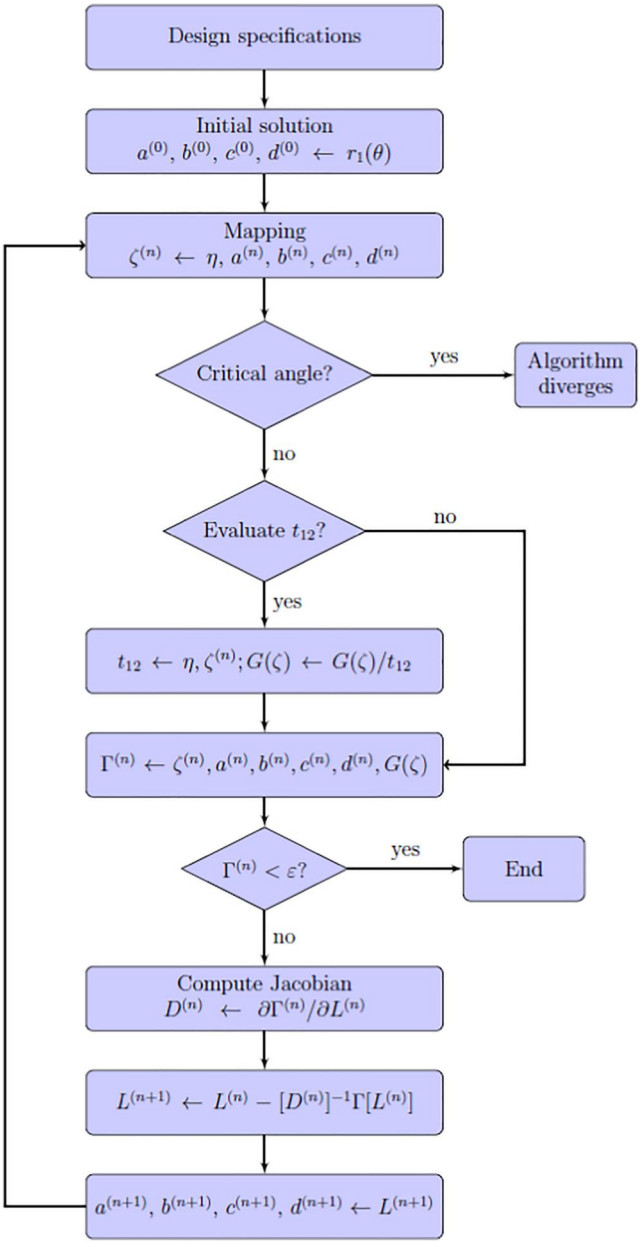

FIGURE 4 Synthesis algorithm.

$$G^S(\zeta) = t_{12}(\theta, \phi)\, G(\zeta) \tag{24}$$

where

$$t_{12}(\eta, \zeta) = \frac{1}{N}\left(A_{\perp}^2 T_{\perp}^2 + A_{//}^2 T_{//}^2\right)\frac{\cos\theta_t}{\cos\theta_i} \tag{25}$$

and $T_{\perp}$,$T_{//}$ are the Fresnel reflection coefficients for a plane wave impinging on the inner surface of the lens with perpendicular and parallel polarisations, respectively:

$$T_{\perp} = \frac{2N(N - \cos\Phi)}{N^2 - 1},\ T_{//} = T_{\perp}\sec\Phi \tag{26}$$

where

$$\cos\Phi = \frac{2\left(\eta\overline{\zeta} + \overline{\eta}\zeta\right) + \left(|\eta|^2 - 1\right)\left(|\zeta|^2 - 1\right)}{\left(|\eta|^2 + 1\right)\left(|\zeta|^2 + 1\right)} \tag{27}$$

and

$$\frac{\cos\theta_t}{\cos\theta_i} = \frac{N\cos\Phi - 1}{N - \cos\Phi} \tag{28}$$

In Eq. (25), functions $A_{\perp}$ and $A_{//}$ depend on the incident field polarisation $\widehat{e}_1$ and, in this work, it is assumed that $\widehat{e}_1 = \cos\phi'\,\widehat{\theta}' - \sin\phi'\,\widehat{\phi}'$, leading to [5]:

$$A_{\perp} = \frac{-j\left(\overline{\zeta} - \overline{\eta}\right)\left(1 + \overline{\zeta}\eta\right) + j(\zeta - \eta) + \left(1 + \overline{\zeta}\eta\right)}{2|\zeta - \eta|\left|1 + \overline{\zeta}\eta\right|} \tag{29}$$

$$A_{//} = -\frac{\left(\overline{\zeta} - \overline{\eta}\right)\left(1 + \overline{\zeta}\eta\right) + (\zeta - \eta) + \left(1 + \overline{\zeta}\eta\right)}{2|\zeta - \eta|\left|1 + \overline{\zeta}\eta\right|} \tag{30}$$

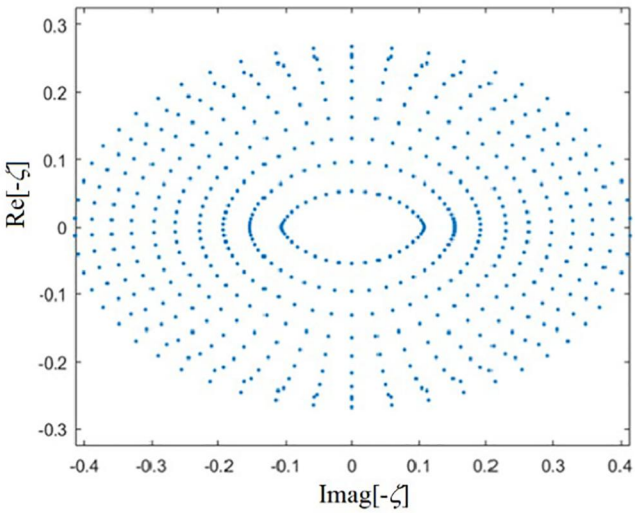

FIGURE 5 Transmitted ray's direction from the synthesised surface in complex plane ζ.

in complex coordinates, where $(A_{\perp})^2 + (A_{//})^2 = 1$.

Function $t_{12}(\eta,\zeta)$ can be used to correct the synthesis specification to achieve the desired far-field power distribution by compensating reflection losses. Using the calculated surface as an initial solution and the distribution we obtained the following equation

$$G'(\zeta) = G_o \frac{G(\zeta)}{t_{12}(\eta,\zeta)} \tag{31}$$

As the new radiated power specification, the solution of the MA equation is again performed, with constant G_o being a normalisation factor to ensure power conservation.

7 | ALGORITHM

Under design specifications, an initial solution is approximated by a set of displaced confocal quadrics over a grid of points. Then, the mapping function $\zeta(\eta)$ given by Equation (5) is analytically evaluated and, if no critical angles occur, the iteration proceeds; otherwise, the algorithm diverges. The iteration proceeds by calculating the reflection losses at the dielectric interface and correcting the desired power density in the far-field region using Equation (31). So, the operator $\Gamma(L)$ and the Jacobian matrix of $\Gamma(L)$ are computed, and a new solution is found by the Newton Method. This new solution is approximated by another set of displaced confocal quadrics

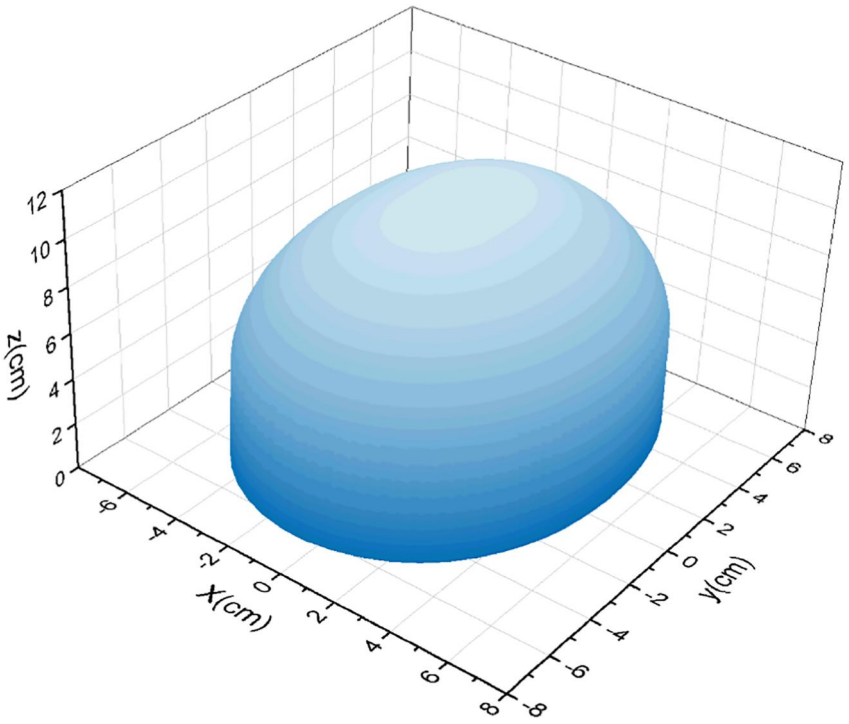

FIGURE 6 3D shape of the synthesised elliptical lens.

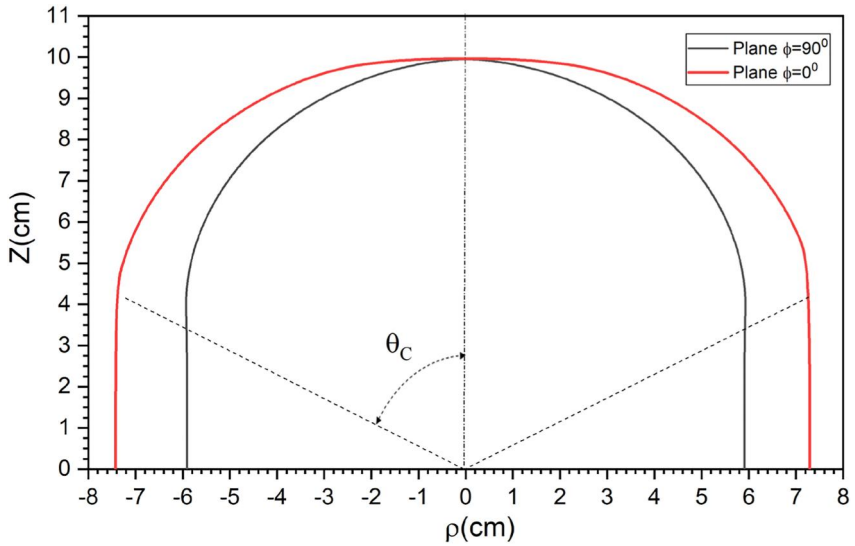

FIGURE 7 Plane cuts of the synthesised elliptical lens.

that is evaluated analytically. The algorithm iterates until the maximum residues of $\Gamma(L)$ is below a specified value. The block diagram of this algorithm is shown in Figure 4.

8 | DESIGN EXAMPLES

To illustrate the effectiveness of the synthesis algorithm in controlling the lens radiated power, we show two design examples chosen to illustrate the formulation's effectiveness. The first case shows the synthesis of an elliptical beam with a Gaussian radiation pattern that collimates the beam in one plane.

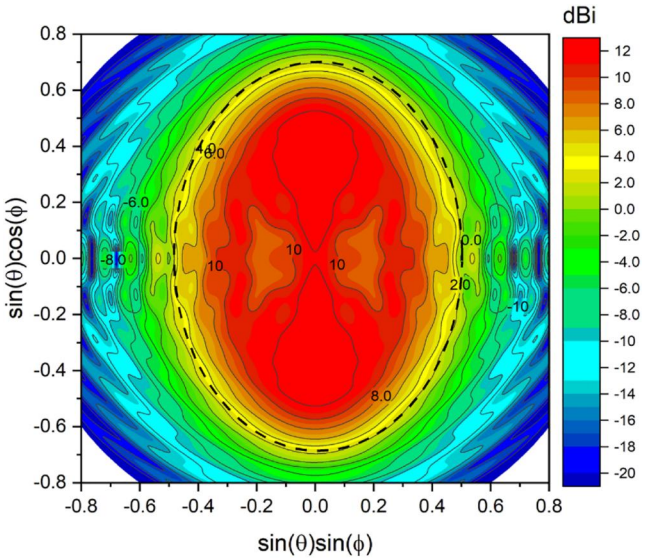

(a)

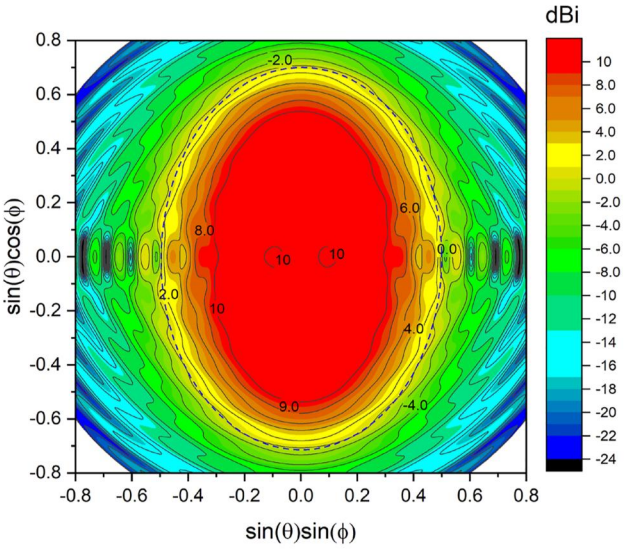

(b)

FIGURE 8 Contour radiation pattern from GO-PO analysis: (a) 30 GHz and (b) 120 GHz.

The second case shows the synthesis of a uniform illumination of a region with a super-elliptical contour, demanding a strong shape on the edge of the lens. For both cases, the antenna lenses operate at 30 GHz, and the thickness along the z-axis is 10 cm ($10\lambda_0$), large enough to apply GO principles. The dielectric lens has a refractive index of $N = 1.6$, corresponding to the electromagnetic relative constants $\varepsilon = 2.56$ and $\mu = 1$. A point source at the origin with an analytical raised-cosine feed model ($I(\theta) = I_0 \cos^n(\theta)$) illuminates the dielectric interface, with the feed cone semi-angle $\theta_c = 60°$. The feed model exponential is $n = 2.8$, yielding −8.5 dB attenuation at θ_c and approximates the radiation pattern provided by a 90° corrugated feed described in Ref. [13] that will be used in the full wave analysis conducted by a CST Studio Suite. To initialise the numerical iterative scheme for the solution of the MA equation, the formulation presented in Ref. [14] was employed to generate a circularly symmetric lens with thickness $Z_A = 10$ cm and designed to radiate a Gaussian beam within a conical region with semi-angle $\alpha = 56°$ and −10 dB attenuation at the edge of the coverage region. To validate the synthesis, the lens radiation pattern was computed by a hybrid technique combining GO and PO approximations, as described in Ref. [5]. For the analysis, a continuous analytical representation of the lens interface was obtained by using pseudo-splines to interpolate the synthesised surfaces' points [15].

8.1 | Case A—Elliptical beam

Case A shows the synthesis of a lens shaped to generate an elliptical beam with the main axis coinciding with the x- and y–axis with widths $\alpha_x = 30°$ and $\alpha_y = 45°$, respectively. The specified radiation pattern $G(\zeta)$ is a Gaussian distribution with edge attenuation of −6 dB at the border of the elliptical coverage region and a maximum gain of 12.59 dBi at boresight. For the synthesis, a non-uniform polar grid in θ, with

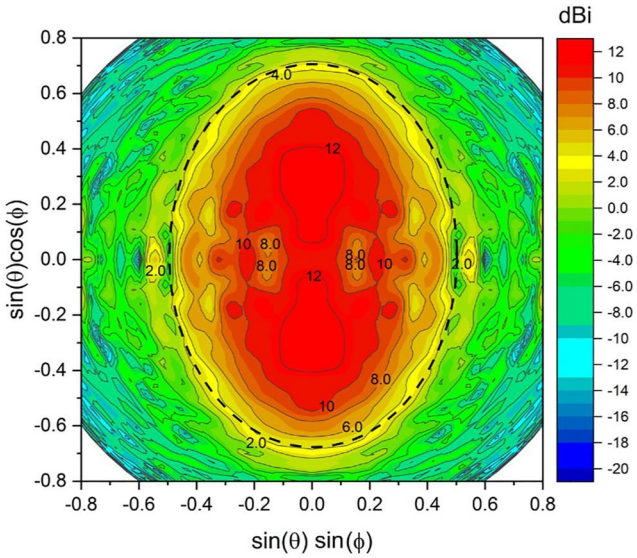

FIGURE 9 Contour radiation pattern from CST analysis at 30 GHz.

$J = 10$ rings and $K = 54$ equally spaced radials, was employed with $\theta_j = \theta_c\,(j/J)^m$ and $m = 0.7$ to concentrate the rings at the edge for better surface description in that region and to ensure convergence of the iterative sequence. Figure 5 shows the grid of ray directions emerging from the synthesised points over the lens surface within the cone of rays defined by θ_c. Figure 6 shows the 3D shape of the lens where a cylinder describes the dielectric interface outside the cone θ_c. The ellipsoidal shape of the synthesised lens is illustrated in Figure 7, which shows plane cuts of the interface at orthogonal planes xz and yz.

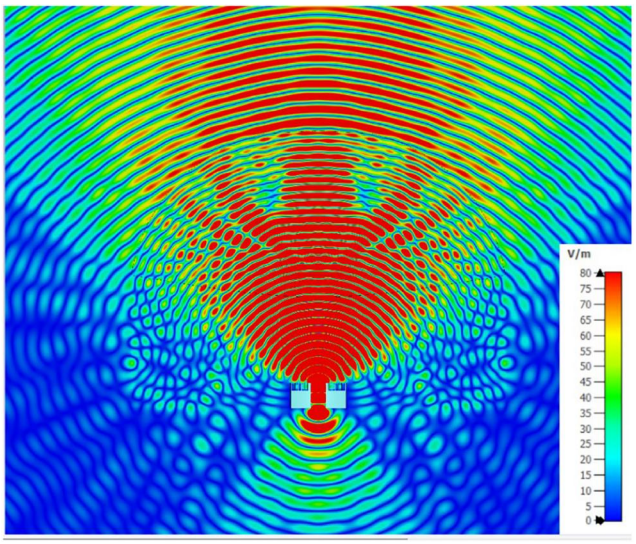

(a)

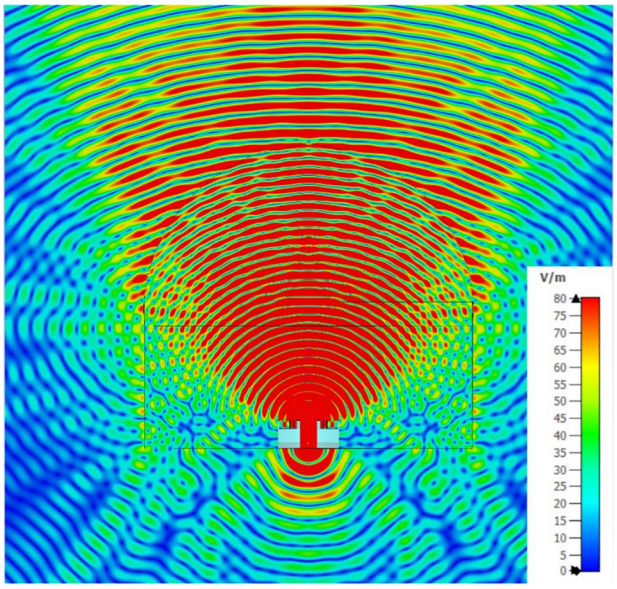

(b)

FIGURE 10 Field distribution inside and outside the lens at 30 GHz: planes (a) $x = 0$ and (b) $y = 0$.

Figure 8a shows the contour plot radiation pattern given by the GO-PO analysis at 30 GHz, where the feed analytical model illuminates the lens. The dashed line describes the far-field boundary imposed in the GO synthesis. Although some oscillation is observed in the central area of the coverage due to diffraction effects not include in the synthesis, below −3 dB the lines follow the desired elliptical shape. To illustrate the numerical convergence of the numerical scheme, Figure 8b shows the GO-PO radiation pattern at 120 GHz, where it is possible to observe the reduction of the oscillations in the main beam and the contour lines acquiring an elliptical shape.

Figure 9 shows the contour plot radiation pattern given by the CST full-wave analysis at 30 GHz, where the 90° corrugated horn illuminates the lens with horn's aperture centre at the origin of the coordinate system [13]. Compared with the results given by the PO-GO analysis in Figure 8a, oscillations increase as some diffractive effects are considered in the full-wave analysis.

Figure 10a,b show the field distribution inside and outside the dielectric lens at planes $x = 0$ and $y = 0$, respectively, where one observes that the radiated beam is narrower at $x = 0$.

8.2 | Case B—Lozenge shaped beam

Case B shows the synthesis of a lens shaped to approximately generate a lozenge coverage described by Equation (24) with $\sigma = 0.7$ and beam widths $\alpha_x = \alpha_y = 30°$. A uniform coverage was specified with a gain of 12.45 dBi. For the synthesis, a non-uniform polar grid in θ, with $J = 10$ rings and $K = 54$ equally spaced radials, was employed with $\theta_j = \theta_c\,(j/J)^m$ and $m = 0.92$ to concentrate rings at the edge for a better description of the lens surface in that region and ensure convergence of the iterative scheme described in Section 7.

Figure 11 shows the grid of ray directions emerging from the synthesised points on the lens surface, where the rings

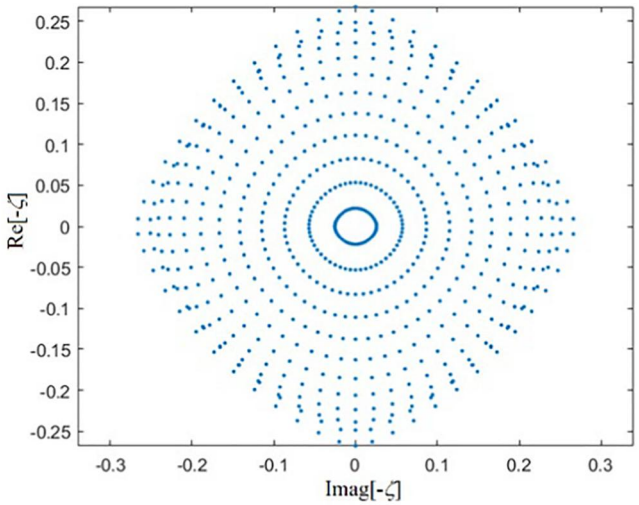

FIGURE 11 Transmitted ray's direction from the synthesised surface in complex plane ζ.

close to the boundary acquire the lozenge shape. In the middle, the rings move to the outer region to redistribute the energy and provide the specified uniform coverage. Figure 12 shows the 3D lens shape with an almost circularly symmetric geometry, where small differences are observed at the boundary in the lens plane cuts shown in Figure 13.

Figure 14a shows the contour plot radiation pattern given by the GO-PO analysis at 30 GHz, together with the boundary of the coverage area described by the dashed line. To illustrate the numerical convergence of the numerical scheme, Figure 14b shows the GO-PO radiation pattern at 120 GHz where it is possible to observe the reduction of the oscillations in the main beam and the contour lines acquiring the desired lozenge shape.

Figure 15 shows the contour plot radiation pattern given by the CST full analysis at 30 GHz, with the 90° corrugated horn illuminating the lens [13].

Figure 16 shows the CST field distribution inside and outside the dielectric lens at plane $x = 0$, from where one observes the radiated beam collimation at 30 GHz, as expected.

9 | CONCLUSIONS

An alternative formulation for the GO synthesis of homogeneous 3D dielectric lens antennas of arbitrary shapes has been presented. It was obtained by imposing GO principles,

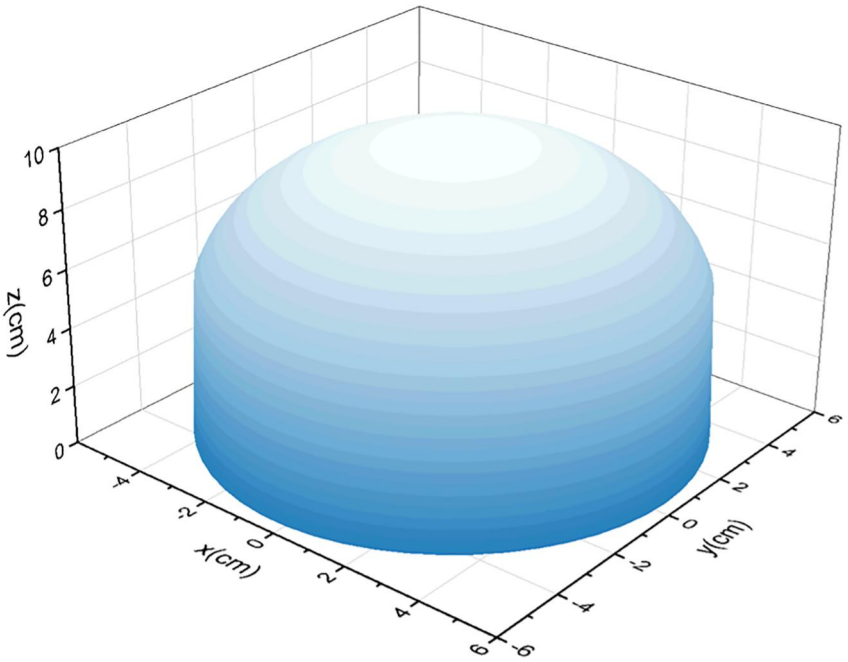

FIGURE 12 3D shape of the synthesised lozenge lens.

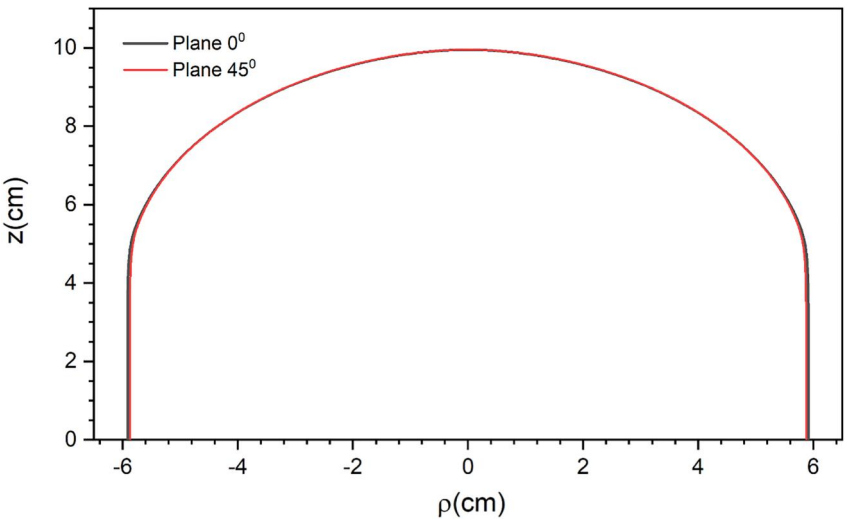

FIGURE 13 Plane cuts of the synthesised lozenge lens.

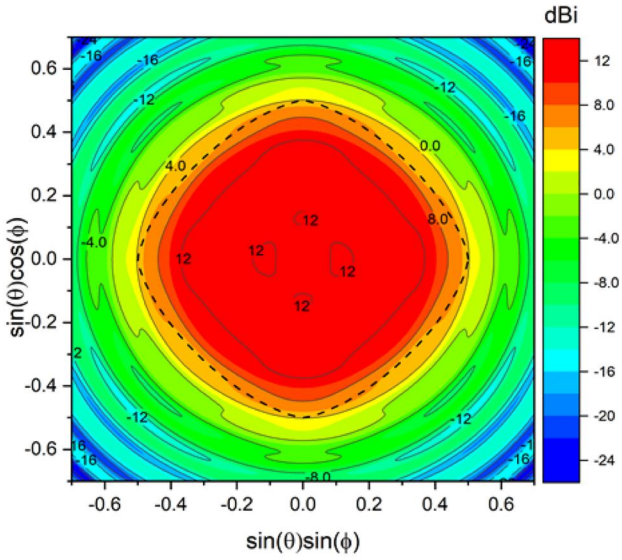

(a)

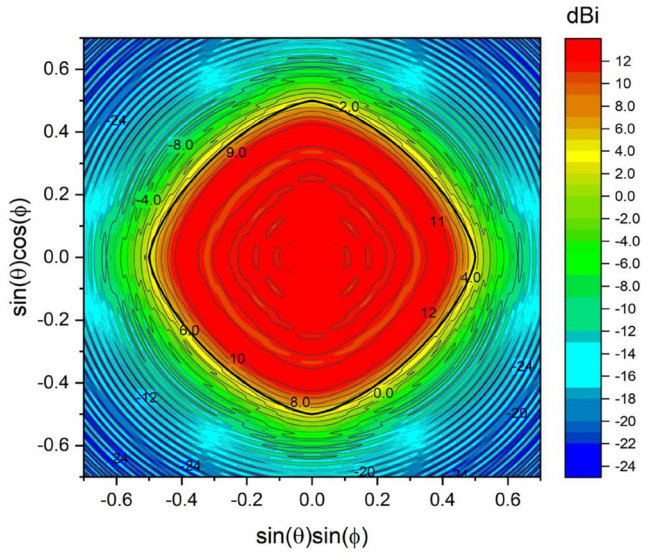

(b)

FIGURE 14 Contour radiation pattern from GO-PO analysis: (a) 30 GHz and (b) 120 GHz.

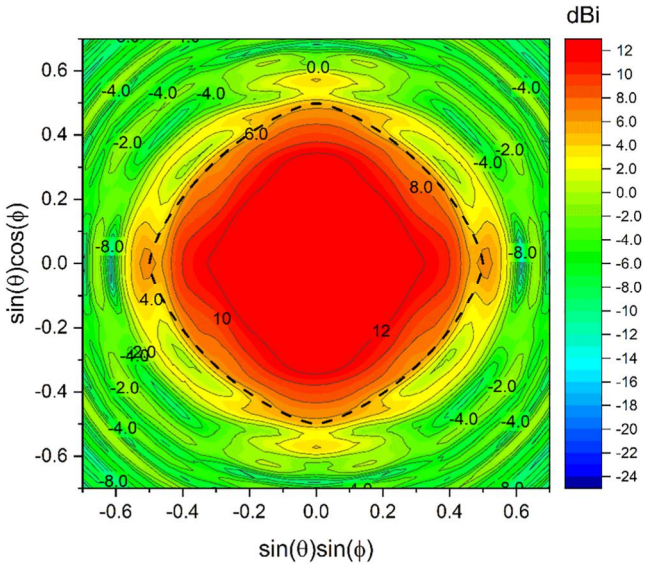

FIGURE 15 Contour radiation pattern from CST analysis at 30 GHz.

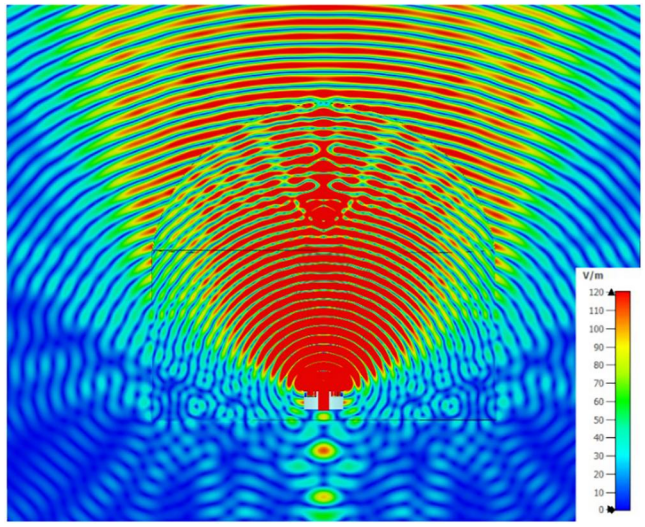

FIGURE 16 Field distribution inside and outside the lens at plane $x = 0$ at 30 GHz.

conservation of energy and Snell's law to the refracted rays at the lens' dielectric interface. Simplification in the formulation was achieved by employing complex coordinates to represent the ray directions. It leads to a non-linear second-order partial differential equation of the MA type that was numerically solved as a boundary value problem. For the task, it was employed as an iterative scheme associated with the use of confocal quadrics to locally represent the lens' interface. Two examples were computed for different boundary coverages and power distributions. The performance of the designs was verified by GO-PO asymptotic analyses and by full-wave analyses performed by CST.

AUTHOR CONTRIBUTIONS

Aline Rocha de Assis: Formal analysis; Investigation; Methodology; Software; Supervision; Writing – original draft. **José Ricardo Bergmann**: Formal analysis; Funding acquisition; Investigation; Methodology; Supervision; Writing – original draft. **Fernando José da Silva Moreira**: Formal analysis; Funding acquisition; Investigation; Methodology; Supervision; Writing – original draft.

ACKNOWLEDGEMENTS

This work was partially supported by CNPq-311249/2021-3, CNPq-303257/2022-9, and FAPEMIG-PPM-384-18.

CONFLICT OF INTEREST STATEMENT

The authors have no conflict of interest to declare.

DATA AVAILABILITY STATEMENT

No data was used for the research described in the article.

PERMISSION TO REPRODUCE MATERIALS

None.

ORCID

José Ricardo Bergmann https://orcid.org/0000-0002-1433-7865
Fernando José da Silva Moreira https://orcid.org/0000-0002-9115-9951

REFERENCES

1. Lee, J.J.: Dielectric lens shaping and coma-correction zoning, part I: analysis. IEEE Trans. Antenn. Propag. 31(1), 211–216 (1983). https://doi.org/10.1109/TAP.1983.1142988
2. Fernandes, C.A., Anunciada, L.M.: Constant flux illumination of square cells for millimeter-wave wireless communications. IEEE Trans. Microw. Theor. Tech. 49(11), 2137–2141 (2001). https://doi.org/10.1109/22.963149
3. Rolland, A., et al.: Axisymmetric resonant lens antenna with improved directivity in Ka-band. IEEE Antenn. Wireless Propag. Lett. 10, 37–40 (2011). https://doi.org/10.1109/LAWP.2011.2109931
4. Boriskin, A., Sauleau, R.: Aperture Antennas for Millimeter and Sub-millimeter Wave Applications. Springer (2018)
5. Chantraine-Bares, B., et al.: A new accurate design method for millimeter-wave homogeneous dielectric substrate lens antennas of arbitrary shape. IEEE Trans. Antenn. Propag. 53(3), 1069–1082 (2005). https://doi.org/10.1109/TAP.2004.842644
6. Brickell, F., Marder, L., Westcott, B.S.: The geometrical optics design of reflectors using complex coordinates. J. Phys. A Math. Gen. 10(2), 245–260 (1977). https://doi.org/10.1088/0305-4470/10/2/014
7. Westcott, B.S., Brickell, F.: Phase and power density distributions on plane aperture of reflector antennas. J. Phys. A Math. Gen. 11(4), 777–789 (1978). https://doi.org/10.1088/0305-4470/11/4/019
8. Westcott, B.S., Stevens, F.A., Brickell, F.: GO synthesis of offset dual reflectors. IEE Proc. H 128(1), 11–18 (1981). https://doi.org/10.1049/ip-h-1.1981.0003
9. Westcott, B.S., Brickell, F.: General dielectric-lens shaping using complex co-ordinates. IEE Proc. H 133(2), 122–126 (1986). https://doi.org/10.1049/ip-h-2.1986.0020
10. Penchel, R.A., Bergmann, J.R., Moreira, F.J.S.: Shaping single offset reflector antennas using local axis-displaced confocal quadrics. Int. J. Antenn. Propag. 2016, Article ID 4715681 (2016). https://doi.org/10.1155/2016/4715681
11. Assis, A.R., Moreira, F.J.S., Bergmann, J.R.: GO synthesis of offset dual reflector antennas using local axis-displaced confocal quadrics. J. Microw. Optoelectron. Electromagn. Appl. 19(2), 177–190 (2020). https://doi.org/10.1590/2179-10742020v19i2813
12. Sokolov, D.D.: Lamé curve. In: Encyclopedia of Mathematics. EMS Press (2001)
13. Resende, U.C., et al.: Evaluation of electromagnetic scattering by conducting bodies of revolution with discontinuous currents. IEEE Trans. Magn. 52(3), Article ID 7200804 (2016). https://doi.org/10.1109/TMAG.2015.2487869
14. Saavedra, L., Bergmann, J.R.: Design of omnidirectinal reflector fed by a dielectric lens associated with a coaxial feed horn. In: 2018 International Conference on Electromagnetics in Advanced Applications (ICEAA), pp. 338–341 (2018). https://doi.org/10.1109/ICEAA.2018.8520358
15. Bergmann, J.R., et al.: A comparison between techniques for global surface interpolation in shaped reflector analysis. IEEE Trans. Antenn. Propag. 42(1), 47–53 (1994). https://doi.org/10.1109/8.272300

How to cite this article: de Assis, A.R., Bergmann, J. R., da Silva Moreira, F.J.: Three-dimensional single-shell dielectric lens design using complex coordinates and local axis-displaced confocal quadrics. IET Microw. Antennas Propag. 17(7), 547–557 (2023). https://doi.org/10.1049/mia2.12365